Transmittance and surface intensity in 3D composite plasmonic waveguides

Alina Karabchevsky,[1,*] **James S. Wilkinson,**[1] **and Michalis N. Zervas**[1]

[1]*Optoelectronics Research Centre, University of Southampton, Southampton, SO17 1BJ, UK*

[*]*A.Karabchevsky@soton.ac.uk*

Abstract: A detailed theoretical study of composite plasmonic waveguide structures is reported. Expressions for modal expansion coefficients, optical transmittance and surface intensity are presented and used to describe the behavior of dielectric channel waveguides containing a short gold-coated section. The superstrate refractive index is shown to control modal beating and modal attenuation in the gold-coated region leading to distinctive features in the surface intensity and device transmittance. The model presented allows detailed prediction of device performance, enabling improved design of highly sensitive miniature devices for evanescent refractometry and vibrational spectroscopy, and can be extended to the design and optimization of composite waveguides structures with nano-patterned overlayers.

OCIS codes: (130.0130) Integrated optics; (130.6010) Sensors; (230.0230) Optical devices; (230.7380) Waveguides, channeled; (240.6680) Surface plasmons.

References and links

1. J. N. Polky and G. L. Mitchell, "Metal-clad planar dielectric waveguide for integrated optics," J. Opt. Soc. Am. B **64**(3), 274–279 (1974).
2. S. Lal, S. Link, and N. J. Halas, "Nano-optics from sensing to waveguiding," Nat. Photon. **1**(11), 641–648 (2007).
3. M. N. Zervas and I. P. Giles, "Performance of surface-plasma-wave fiber-optic polarizers," Opt. Lett. **9**(15), 513–515 (1990).
4. H. J. M. Kreuwel, P. V. Lambeck, J. M. M. Beltman, and Th. J. A. Popma, "Mode coupling in multilayered structures applied to a chemical sensor and a wavelength-selective directional couplers," in *Proceedings of Fourth European Conference on Integrated Optics* (ECIO, 1987), pp. 171–220.
5. F. Peyskens, A. Z. Subramanian, A. Dhakal, N. Le Thomas, and R. Baets, "Enhancement of Raman scattering efficiency by a metallic nano-antenna on top of a high index contrast waveguide," in *Proceeding of Conference on Lasers and Electro-Optics* (CLEO, 2013), pp. 1–2.
6. S. J. Pearce, M. E. Pollard, S. Oo, R. Q. Chen, S. Kalsi, and M. D. B. Charlton, "Integrated waveguide and nanostructured sensor platform for surface-enhanced Raman spectroscopy," J. Nanophoton. **8**(1), 1–11 (2014).
7. R. Quidant, C. Girard, J. C. Webber, and A. Dereux, "Tailoring the transmittance of integrated optical waveguides with short metallic nanoparticle chains," Phys. Rev. B **69**(085407), 1–7 (2004).
8. O. Tokel, F. Inci, and U. Demirci, "Advances in plasmonic technologies for point of care applications," Chem. Rev. **114**(11), 5728–5752 (2014).
9. H. Raether, *Surface Plasmons on Smooth and Rough Surfaces and on Gratings* (Springer-Verlag, 1988).
10. J. Čtyroký, J. Homola, P. V. Lambeck, S. Musa, H. J. W. M. Hoekstra, R. D. Harris, J. S. Wilkinson, B. Usievich, and N. M. Lyndin, "Theory and modelling of optical waveguide sensors utilising surface plasmon resonance," Sensor. Actuat. B-Chem. **54**(1-2), 66–73 (1999).
11. R. Levy and S. Ruschin, "SPR waveguide sensor based on transition of modes at abrupt discontinuity," Sensor. Actuat. B-Chem. **124**(2), 459–465 (2007).
12. M. L. Nesterov, A. V. Kats, and S. K. Turitsyn, "Extremely short-length surface plasmon resonance devices," Opt. Express **16**(25), 20228–20240 (2008).
13. J. Shibayama, "Numerical analysis of waveguide-based surface plasmon resonance sensors with adsorbed layer using two- and three-dimensional beam-propagation methods," IEICE Trans. Electron. **E90-C**(1), 95–101 (2007).

#235802 - $15.00 USD Received 11 Mar 2015; revised 8 May 2015; accepted 15 May 2015; published 22 May 2015

14. J. Shibayama, "Three-Dimensional numerical investigation of an improved surface plasmon resonance waveguide sensor," IEEE Photon. Technol. Lett. **22**(9), 643–645 (2010).
15. J. Čtyroký, J. Homola, and M. Skalsky, "Modelling of surface plasmon resonance waveguide sensor by complex mode expansion and propagation method," Opt. Quant. Electron. **29**(2), 301–311 (1997).
16. R. D. Harris, B. J. Luff, J. S. Wilkinson, J. Piehler, A. Brecht, G. Gauglitz, R. A. Abuknesha, "Integrated optical surface plasmon resonance immunoprobe for simazine detection," Biosens. Bioelectron. **14**(4), 377–386 (1999).
17. P. Berini, "Long-range surface plasmon polaritons," Adv. Opt. Photonics **1**(3), 484–588 (2009).
18. J. J. Burke, G. I. Stegeman, and T. Tamir, "Surface-polariton-like waves guided by thin, lossy metal films," Phys. Rev. B **33**(8), 5186–5201 (1986).
19. J. A. Dionne, L. A. Sweatlock, H. A. Atwater, and A. Polman, "Planar metal plasmon waveguides: frequency-dependent dispersion, propagation, localization, and loss beyond the free electron model," Phys. Rev. B **72**(075405), 1–11 (2005).
20. A. Otto, "Excitation by light of ω_+ and ω_- surface plasma waves in thin metal layers," Z. Phys. **219**(4), 227-233 (1969).
21. A. F. Milton and W. K. Burns, "Mode coupling in optical waveguide horns," IEEE J. Quantum Electron. **13**(10), 828–835 (1977).
22. R. Wan, F. Liu, Y. Huang, and J. Peng, "Vertical coupling between short range surface plasmon polariton mode and dielectric waveguide mode," Appl. Phys. Lett. **94**(141104), 1–3 (2009).
23. F. Liu, R. Wan, Y. Huang, and J. Peng, "Refractive index dependence of the coupling characteristics between long-range surface-plasmon-polariton and dielectric waveguide modes," Opt. Lett. **34**(17), 2697–2699 (2009).
24. R. Wan, F. Liu, and Y. Huang, "Ultrathin layer sensing based on hybrid coupler with short-range surface plasmon polariton and dielectric waveguide," Opt. Lett. **35**(2), 244–246 (2010).
25. M. N. Zervas, "Surface plasmon-polariton fiber-optic polarizers using thin-nickel films," IEEE Photon. Technol. Lett. **2**(4), 253–256 (1990).
26. M. N. Zervas, "Surface plasmon-polariton fiber-optic polarizers using thin-chromium films," IEEE Photon. Technol. Lett. **2**(8), 597-599 (1990).
27. D. Sarid, "Long-range surface-plasma waves on very thin metal films," Phys. Rev. Lett. **48**(26), 1927–1930 (1981).
28. M. N. Zervas, "Surface plasmon-polariton waves guided by thin metal films," Opt. Lett. **16**(10), 720–722 (1991).
29. F. Y. Kou and T. Tamir, "Range extension of surface plasmons by dielectric layers," Opt. Lett. **12**(5), 367–369 (1987).
30. R. F. Oulton, V. J. Sorger, D. A. Genov, D. F. P. Pile, and X. Zhang, "A hybrid plasmonic waveguide for subwavelength confinement and long-range propagation," Nat. Photon. Lett. **2**(8), 496–500 (2008).
31. S. J. Al-Bader, "Optical transmission on metallic wires - fundamental modes," IEEE J. Quantum Electron. **40**(3), 325-329 (2004).
32. R. Zia, M. D. Selker, and M. L. Brongersma, "Leaky and bound modes of surface plasmon waveguides," Phys. Rev. B. **71**(165431), 1–9 (2005).
33. R. Zia, A. Chandran, and M. L. Brongersma, "Dielectric waveguide model for guided surface polaritons," Opt. Lett. **30**(12), 1473-1475 (2005).

1. Introduction

Hybrid plasmonic devices incorporating dielectric and metallic waveguiding structures [1, 2] offer great potential for ultra-compact high performance devices from polarizers [3] and sensors [4], through surface-enhanced Raman spectrometers [5,6], to telecommunications filters [7] and all-optical switches. In particular there is growing interest in such plasmonic technologies for biochemical analysis in clinical point-of-care applications [8].

Several theoretical approaches have been employed to model and design these devices for the case of waveguide sensors using surface plasmon resonance (SPR). Surface plasmons (surface plasma charges oscillations) are electron charges on a metal boundary which can perform coherent fluctuations [9]. Initially, simple, fast approaches to modeling 2D (metal-coated slab) waveguide structures were adopted to study the coupling behavior between dielectric and plasmonic waveguides and to predict refractometric sensor performance [10–13]. The use of channel dielectric waveguides is more practical as they allow for compactness and integration of multiple on-chip functionalities. The different characteristics of channel waveguide modes compared with slab waveguide modes in terms of field components and distributions and modal velocities mean that more sophisticated 3D models are required for accurate design

#235802 - $15.00 USD Received 11 Mar 2015; revised 8 May 2015; accepted 15 May 2015; published 22 May 2015

and fuller understanding of channel waveguide based devices. Several approaches have been adopted to model 3D composite plasmonic waveguide devices including the beam propagation method [13, 14]. The beam propagation method 3D approach follows the results obtained by 2D beam propagation method approach having wide enough overlayer which covers the core region. However, it does not yield detailed information on the nature and excitation of the various modes throughout the structure. An understanding of these modes is important for the design of more advanced devices, such as devices with complex nanopatterned metal structures for ultrasensitive surface spectroscopy, refractometry and sensing. In this paper we present a detailed analysis of the excitation and propagation of modes in channel photonic waveguides overlaid with a short section of a noble metal plasmonic overlayer as schematically depicted on Fig. 1(a). The orthogonality of complex modes in the noble metal coated region, excited from the monomode dielectric region, leads to explicit expressions for the expansion coefficients coupling the modes between the regions [15]. The modal properties, i.e. field distributions and complex propagation constants, of the uncoated and metal-coated channel waveguide sections have been determined using a commercial finite-element method (FEM) package (COMSOL) fully controlled by Matlab, using similar design values as [10] for comparison. The analysis presented in this paper extends the results of [10] from the slab waveguide geometry to the more realistic channel waveguide geometry [16] and explores the resultant behavior of the expansion coefficients, modal interference and surface intensity distributions not discussed in [10]. These have then been used to illustrate the behavior of the complex expansion coefficients into and out of the metal coated region, which are discussed in terms of power conservation. Using this approach, the transmittance of such a channel waveguide SPR refractometer is calculated as a function of the refractive index of the superstrate. Future compact devices for surface-enhanced sensing will rely upon high surface intensity over short lengths for efficient operation. Our model is used to determine the optical intensity at the surface of the noble metal film along the length of the waveguide, by superposition of the modes, which carry modal powers calculated according to their expansion coefficients. The contribution of each of the modes in the metal-coated region is discussed and the mode-beating behavior, which leads to short regions of high surface intensity, is described. The method presented here elucidates the behavior of the complex expansion coefficients between waveguide sections for absorbing materials, develops a detailed understanding of the modal behavior in noble-metal coated dielectric waveguides and provides an accurate design approach for future composite plasmonic waveguides and nanopatterned devices for field localization.

2. 3D composite plasmonic waveguide analysis

Surface plasmon-polaritons (SPP) are supported by several different optical waveguide configurations [17]. Thin metal films sandwiched between two semi-infinite dielectric media are known to support bound and a leaky SPP modes with symmetric and anti-symmetric transverse-magnetic field distributions across the film thickness [18, 19]. Bound or leaky modes can be preferentially excited by controlling the coupling conditions [9, 20], and surrounding refractive indices [3–15, 17–26]. It is also known that symmetric-bound SPP modes show the lowest propagation losses and longest propagation distances, and are therefore termed long-range SPPs, in quasi-symmetric [27], as well as, highly asymmetric [28] thin metal film structures. The propagation distance can be extended substantially by bringing the SPP-supporting thin metal film in close proximity to a planar dielectric waveguide [29]. In this case, in addition to symmetric and anti-symmetric bound SPP modes, the composite structure supports hybrid modes [30] resulting from combinations between dielectric and SPP modes. The extended range SPP mode is a hybrid mode, which is a combination of the dielectric and the symmetric-bound SPP mode, with the majority of the electromagnetic (EM) energy contained within the dielectric waveg-

#235802 - $15.00 USD Received 11 Mar 2015; revised 8 May 2015; accepted 15 May 2015; published 22 May 2015

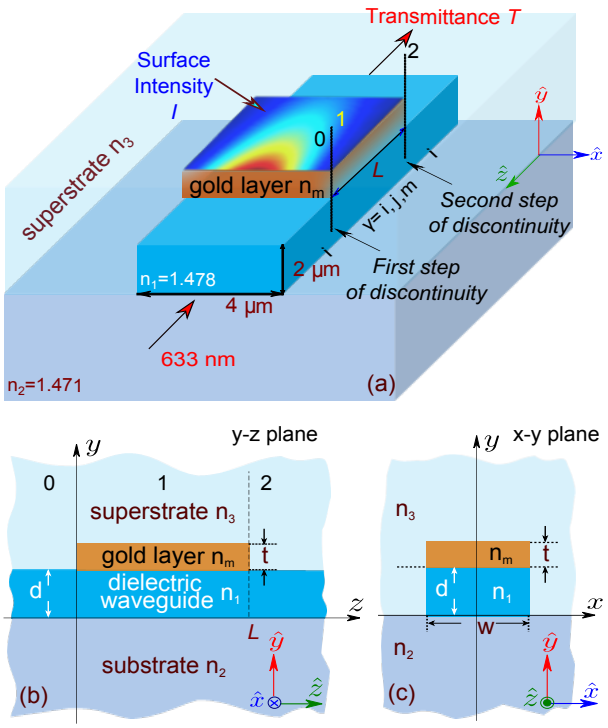

Fig. 1. (a) 3D schematic of composite plasmonic waveguide and its cross-sections in the (b) (y-z) plane and (c) (x-y) plane (dimensions are shown out of scale).

uide showing only a small overlap with the adjacent thin metal film. It is precisely this minimum overlap of the EM field with the lossy thin metal film that results in the extended range of the hybrid modes. However, in this case, the increased propagation distance is inevitably achieved at the expense of the top-surface intensity.

A number of different methods have been used to excite SPPs including grating approaches [9] and prism-based [9, 18] approaches. They include prism coupling with attenuated total-internal reflection (ATR) in the Otto [20] or Kretschmann-Raether [9] configurations, evanescent field coupling [3, 25, 26], and end-firing [18]. While ATR and evanescent methods require exact phase matching for efficient SPP excitation, end-firing requires only field matching of the mode in question at the excitation point and it is, therefore, much more versatile. For example, the Kretschmann configuration can never excite purely bound modes. On the other hand, devices based on evanescent wave coupling rely on efficient excitation of symmetric bound or leaky modes, depending on the superstrate refractive index [3,25,26]. Controlling the excitation of the appropriate SPP mode is of paramount importance for optimising the performance of the optical devices.

2.1. 3D plasmonic mode configuration - mode field distributions and dispersion curves

The 3D composite plasmonic waveguide considered in this study is shown in Fig. 1(a) and is modelled throughout at a wavelength of 633nm. It consists of a dielectric rib waveguide with core having index of $n_1 = 1.478$, width of 4μm and height of 2μm, covered by a $50nm$ thick gold stripe with complex index of $0.197 - 3.466j$ [10] over a finite length L, the refractive index of the substrate $n_2 = 1.471$. The superstrate index was chosen to vary from 1.3

#235802 - $15.00 USD Received 11 Mar 2015; revised 8 May 2015; accepted 15 May 2015; published 22 May 2015

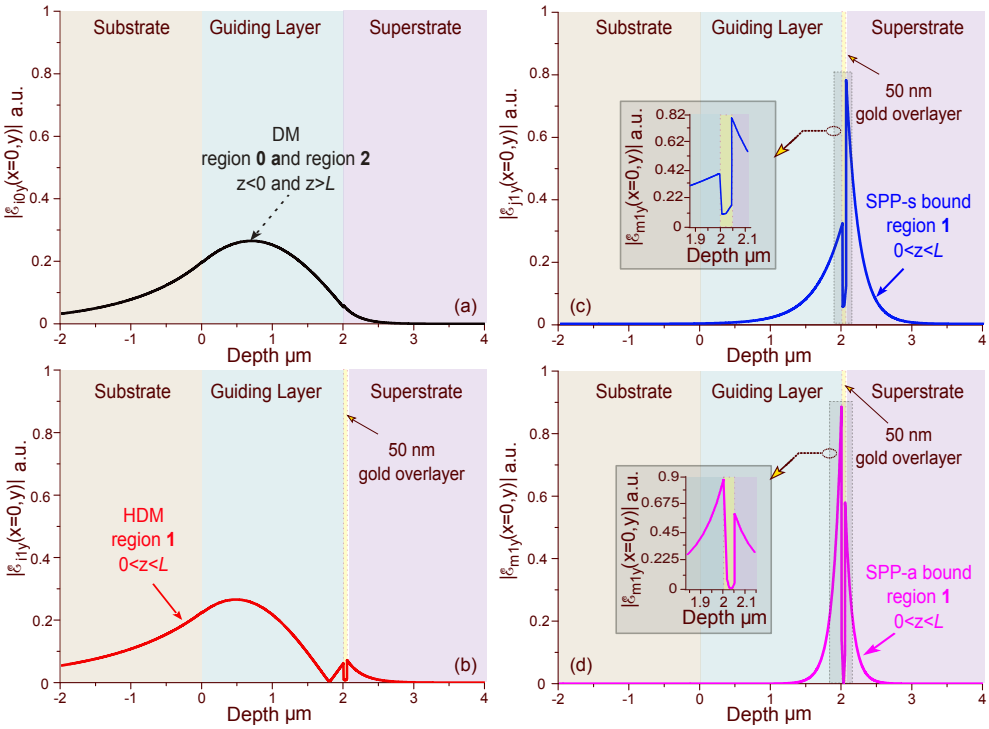

Fig. 2. Cross-sections of the y-component of the electric field magnitude for the structure with a superstrate index of 1.4 in (a) a purely dielectric mode (DM) in a dielectric waveguide in the $z < 0$ and $z > L$ regions. In a (b-d) the gold coated $0 < z < L$ region (b) hybrid dielectric/plasmonic mode (HDM), (c) SPP-s and (d) SPP-a bounds have been calculated by the FEM using COMSOL 4.3b with Matlab module. Insets (c) and (d) show the zoomed gold region and nearby regions.

to 1.44 to cover important aqueous analytes such as soft drinks, or those encountered in immunoassays [16]. The superstrate index values used were chosen to illustrate the behavior of the modes and modal excitation close to and far from the surface plasmon resonance; in practice very small changes in refractive index can be achieved by altering the sucrose content of aqueous solutions. These values are taken from [10] for ease of comparison of slab and channel waveguide behavior. The waveguide refractive index values and dimensions are a good approximation to the K^+ ion-exchanged waveguides used in [16], and correspond to a typical index contrast yielding monomode operation with good modal compatibility with optical fiber for connection to instrumentation. Figures 1(b)-1(c) show the composite plasmonic waveguide cross-sections in the (y-z) and (x-y) planes respectively. Thin metallic stripe plasmonic waveguides are shown to support symmetric and anti-symmetric bound and leaky modes, as well as corner modes [31, 32]. Here symmetric and anti-symmetric modes have been defined from the real and imaginary $\mathscr{E}_y$ field component with respect to the centre of the gold strip (similar to symmetric and anti-symmetric modes defined from real and imaginary $\mathscr{H}_y$ field component in Fig. 2 in [10]. In analogy with planar geometries [29], the composite 3D structure, including the dielectric rib waveguide, is expected to support additional hybrid modes. The supported guided and leaky modes of the 3D composite waveguide have been calculated using FEM based COMSOL 4.3b with Matlab module.

Figure 2 shows cross sections of the dominant y-component of the electric field magnitude

#235802 - $15.00 USD Received 11 Mar 2015; revised 8 May 2015; accepted 15 May 2015; published 22 May 2015

supported by the dielectric waveguide, Fig. 2(a) and composite plasmonic waveguide in Figs. 2(b)-2(d). The fields are plotted across the waveguide center along the y (depth) direction in the (y-z) plane. Figure 2(a) shows the field profile of the purely dielectric mode (DM) supported by the monomode dielectric waveguide in the $z < 0$ and $z > L$ regions. Figures 2(b) shows the profile of the fundamental hybrid dielectric/plasmonic (HDM) mode supported by the composite dielectric/plasmonic waveguide for $0 < z < L$. HDM results as a combination of DM and a symmetric SPP mode supported by the adjacent thin metal ridge waveguide. Figures 2(c)-2(d) on the other hand show the profiles of the SPP symmetric (SPP-s) and anti-symmetric (SPP-a) bound modes, supported primarily by the thin metal ridge waveguide. In addition to bound SPP-a, the structure supports a leaky SPP-s as shown in Fig. 3(g).

The optical properties and characteristics of the modes, such as the field distributions and propagation constants, depend on the parameters of the waveguide structure. Figure 3 shows typical distributions of the dominant electric field component $\mathscr{E}_y$ for DM, Figs. 3(a)-3(c), HDM Figs. 3(d)-3(f), SPP-s Figs. 3(g)-3(i), and SPP-a Figs. 3(k)-3(m). The fields correspond to three different superstrate indices. It is shown that the modes are localized in different areas of the waveguide cross-section and their overall field distribution is affected by the superstrate index to a different extent.

Figure 4(a) shows the variation of the effective index N_{eff} as a function of the superstrate index where:

$$N_{eff} = \Re(\beta)\lambda/(2\pi) \tag{1}$$

Where $\Re(\beta)$ is the real part of the complex propagation constant β. SPP-a is of high effective index compared to HDM. The index of the SPP-s strongly depends on the refractive index of the superstrate. The results of the current 3D composite waveguide are compared with their counterparts supported by a similar 2D planar waveguide [10] showing excellent agreement. This is not surprising, since the dispersion of surface modes supported by 2D stripe plasmonic waveguides are well described by 1-D slab counterparts [13,33]. Figure 4(c) shows an expanded version of the dispersion curves for the effective refractive index of HDM and SPP-s around the resonance. The resonance occurs when the DM matches the SPP-s mode. The effective indices of the HDM and SPP-s modes diverge strongly away from the resonance at $n_3 = 1.365$. Index difference between effective refractive indices of a HDM and SPP-s on Fig. 4(a) excited in a gold coated region $0 < z < L$ is more pronounced, starting from the resonance. Below the resonance SPP-s radiates into the substrate Fig. 3(d) with highest losses for the structure having a superstrate of low index (lower than resonance which occurs at 1.365 of the superstrate), Fig. 3(e). However, above the resonance, SPP-s is confined by the metal strip. The dispersion of the HDM can be explained by the distribution of the normalized time averaged energy density.

Figure 4(b) shows variation of attenuation coefficient α in dB/cm of modes in a gold coated region $0 < z < L$ with superstrate index calculated according to Eq. (2):

$$\alpha = 0.2\log(e)\Im(\beta) \tag{2}$$

Where $\Im(\beta)$ is the imaginary part of the complex propagation constant β. SPP-s and SPP-a exhibit high modal attenuation. Zones I, II and III in Fig. 4(b) indicate superstrate indices below, near, and above resonance which will be discussed in terms of modal interference behavior in Sections 3.2 and 3.3. The HDM shows a high loss around the resonance and low loss far from it suggesting that waveguide transmittance will be predominantly defined by the imaginary part of the propagation constant $\Im(\beta)$ of this mode.

Figure 4(c) shows details of the effective index variations of the DM, HDM and SPP-s modes. The effective index of the HDM varies slightly over the entire range of superstrate indices and

#235802 - $15.00 USD Received 11 Mar 2015; revised 8 May 2015; accepted 15 May 2015; published 22 May 2015

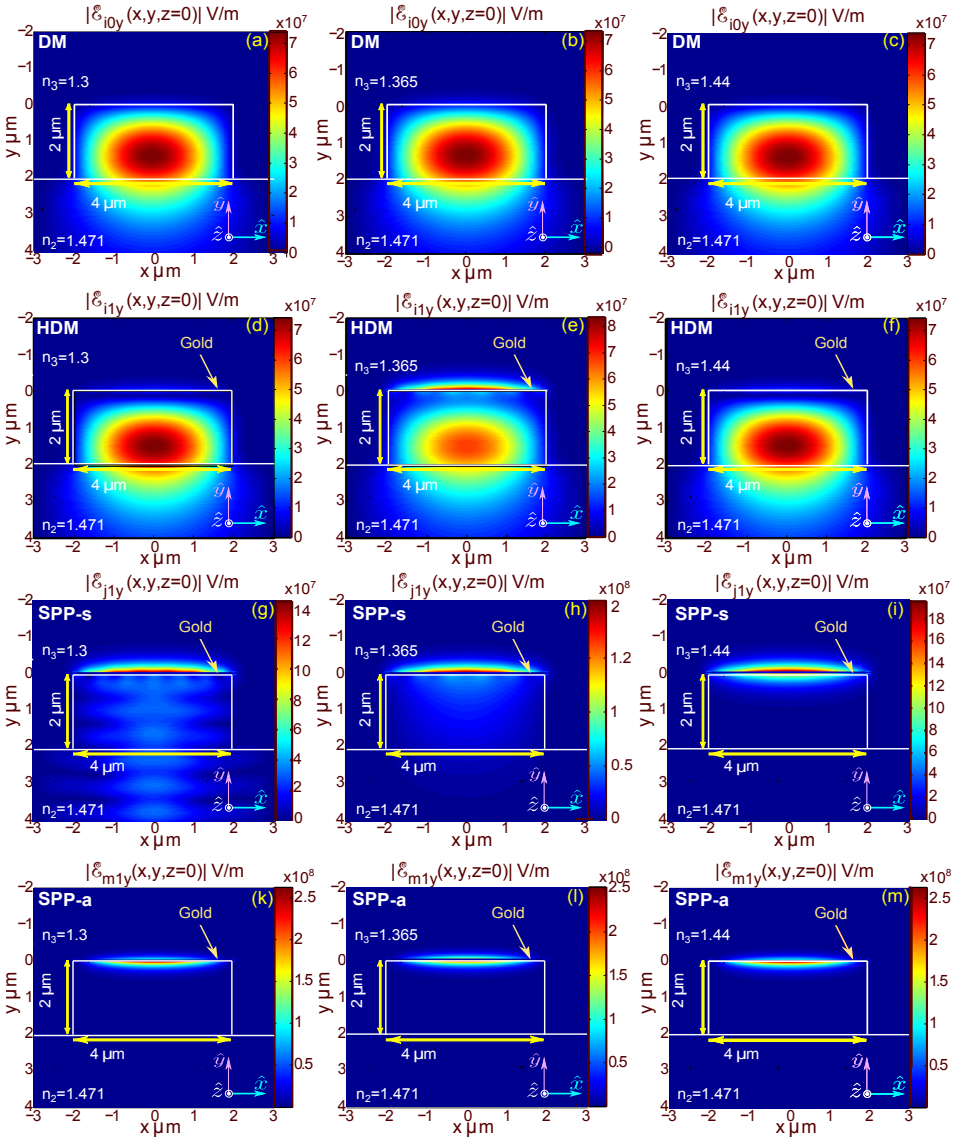

Fig. 3. Evolution of the dominant y-component of electric field magnitudes for quasi-transverse magnetic modes at resonance having superstrate index of 1.365, and far from it, at low superstrate index: 1.3 and high superstrate index 1.44 as labeled on the figure accordingly for DM, HDM, SPP-s and SPP-a guided modes.

#235802 - $15.00 USD Received 11 Mar 2015; revised 8 May 2015; accepted 15 May 2015; published 22 May 2015

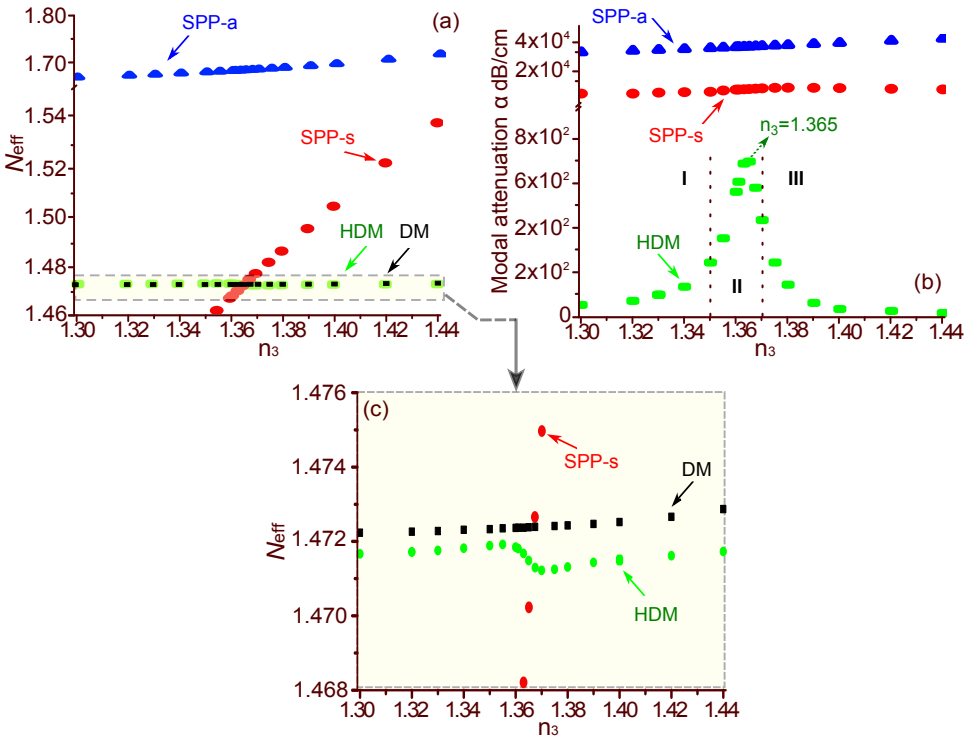

Fig. 4. Variation of (a) effective refractive indices and (b) modal attenuation coefficients α in the gold-coated region $0 < z < L$ with n_3; (c) zoomed effective indices in the region enclosed in (a). Note: The superstrate index, n_3 of maximum HDM propagation loss is labelled in (b).

remains close to the effective index of the DM. This is expected, since HDM is predominantly localized within the dielectric waveguide, similarly with DM, compare Figs. 3(a)-3(f). The HDM mode propagation loss, on the other hand, although the lowest, shows a resonant increase around a superstrate index of 1.365. At this superstrate index, DM and SPP-s are phase-matched and as a result the HDM, which is an anti-symmetric linear combination of DM and SPP-s, overlaps substantially with the metallic strip as shown in Fig. 2(e). Although DM and SPP-s modes propagate independently having their own propagation constants, the propagation constants are similar at the resonance and also close to that of HDM. Non-monotonic variation of effective index of HDM near the resonance occurs due to the non-monotonic variation of its propagation constant. The effective indices and propagation losses of SPP-s and SPP-a, on the other hand, vary linearly with superstrate index (note the scale change). This behavior is similar to that shown by similar modes supported by thin metallic films [28]. It should be noted that for low superstrate indices no bound SPP-s mode exists and the supported mode is leaky.

2.2. *Mode-matching conditions at waveguide discontinuities*

The excitation of the modes at the beginning of the gold-coated region (1), by the mode of the input region (0) to determine the fields of the entire composite waveguide is achieved by applying appropriate mode-matching conditions at the input ($z = 0$) and output ($z = L$) interfaces of the dielectric rib waveguide and the composite dielectric/metallic stripe waveguide. We assume guided pure dielectric mode, DM, in Fig. 2(a) designated by a subscript $i0$ in the input:

#235802 - $15.00 USD Received 11 Mar 2015; revised 8 May 2015; accepted 15 May 2015; published 22 May 2015

region 0 in Fig. 1 and output: Region 2 on Fig. 1 side (pure dielectric waveguide) of the first step and orthogonal guided modes $\gamma 1 = i1, j1$ or $m1$ assigned to HDM in Fig. 2(b), SPP-s, in Fig. 2(c) and SPP-a in Fig. 2(d) modes, respectively, in the output side (dielectric waveguide with plasmonic overlayer) of the first step as shown in Fig. 1(a) with quasi-transverse magnetic components. At $z = 0$, the general complex field distributions at the boundary between region 0 and region 1, ignoring the reflected and radiated modes, are:

$$E_{\xi i0} = \sum_{\gamma=i,j,m} E_{\xi\gamma 1};\ H_{\xi i0} = \sum_{\gamma=i,j,m} H_{\xi\gamma 1}. \tag{3}$$

Where $\xi = x, y$ and $\mathbf{E} = E_x\widehat{x} + E_y\widehat{y} + E_z\widehat{z}$ and $\mathbf{H} = H_x\widehat{x} + H_y\widehat{y} + H_z\widehat{z}$. $\widehat{x}$, $\widehat{y}$ and $\widehat{z}$ are unit vectors in the x, y and z directions respectively. An expression for the expansion coefficient between input mode $i1$ in region 0 and mode $j1$ in region 1 is derived using the complex orthogonality principle:

$$\int_{-\infty}^{\infty}\int_{-\infty}^{\infty}(\mathbf{E}_{i0}\times\mathbf{H}_{\gamma 1})_z + (\mathbf{E}_{\gamma 1}\times\mathbf{H}_{i0})_z \mathrm{dxdy} = \int_{-\infty}^{\infty}\int_{-\infty}^{\infty}(\mathbf{E}_{\gamma 1}\times\mathbf{H}_{\gamma 1})_z + (\mathbf{E}_{\gamma 1}\times\mathbf{H}_{\gamma 1})_z \mathrm{dxdy} \tag{4}$$

Where $\gamma 1 = i1, j1, m1$. We now express a general complex electric and magnetic field distribution components:

$$\mathbf{E}_\delta(x,y,z) = a_\delta \bar{\mathscr{E}}_\delta(x,y) exp(-j\beta_\delta z) \tag{5}$$

$$\mathbf{H}_\delta(x,y,z) = a_\delta \bar{\mathscr{H}}_\delta(x,y) exp(-j\beta_\delta z) \tag{6}$$

Where β_δ is the propagation constant of mode δ. $\bar{\mathscr{E}}_\delta(x,y,z)$ and $\bar{\mathscr{H}}_\delta(x,y,z)$ are extracted complex vectorial electric and magnetic field components calculated using FEM and $\bar{\mathscr{E}} = \mathscr{E}_x\widehat{x} + \mathscr{E}_y\widehat{y} + \mathscr{E}_z\widehat{z}$ and $\bar{\mathscr{H}} = \mathscr{H}_x\widehat{x} + \mathscr{H}_y\widehat{y} + \mathscr{H}_z\widehat{z}$. $a_\delta = N_\delta A_\delta = E_\delta(x,y,z)/(\mathscr{E}_\delta(x,y)exp(-j\beta_\delta z)) = H_\delta(x,y,z)/(\mathscr{H}_\delta(x,y)exp(-j\beta_\delta z))$ and A_δ is complex, $A_\delta = |A_\delta| exp(-j\phi_\delta)$ related to the power carried by the mode as: $P_\delta = |A_\delta|^2$. The normalization factor N_δ giving rise to each mode carrying unity power, $P_\delta = 1$ is: $N_\delta = (2/\Re(\int_{-\infty}^{\infty}\int_{-\infty}^{\infty}(\bar{\mathscr{E}}_\delta \times \bar{\mathscr{H}}^*{}_\delta)_z \mathrm{dxdy}))^{1/2}$.

For $z = 0$ these are:

$$a_{i0}\mathscr{H}_{\xi i0} = \sum_{\gamma=i,j,m} a_{\gamma 1}\mathscr{H}_{\xi\gamma 1};\ a_{i0}\mathscr{E}_{\xi i0} = \sum_{\gamma=i,j,m} a_{\gamma 1}\mathscr{E}_{\xi\gamma 1}. \tag{7}$$

Power in any region is defined as:

$$P = 1/2\Re\int_{-\infty}^{\infty}\int_{-\infty}^{\infty}(\bar{\mathscr{E}}\times\bar{\mathscr{H}}^*)_z \mathrm{dxdy}. \tag{8}$$

A relation between eigenmodes at an abrupt step is detailed in Appendix.

An expansion coefficient $c_{i0,\gamma 1}$ expanding mode $i1$ from region 0 into mode $\gamma 1$ in region 1 over the first abrupt step is:

$$c_{i0,\gamma 1} = a_{\gamma 1}/a_{i0} = N_{i0}(I_{i0,\gamma 1} + I_{\gamma 1,i0})/(2I_{\gamma 1,\gamma 1}N_{\gamma 1}) \tag{9}$$

At $z = L$, the expansion coefficients are derived in a similar manner to that detailed above resulting in:

$$c_{\gamma 1,i2} = (I_{\gamma 1,i2} + I_{i2,\gamma 1})\exp(-j(\beta_{\gamma 1} - \beta_{i2})L)/(2I_{i2,i2}) \tag{10}$$

Since, $a_{\gamma 1} = c_{i0,\gamma 1}a_{i0}$

#235802 - $15.00 USD Received 11 Mar 2015; revised 8 May 2015; accepted 15 May 2015; published 22 May 2015

$$a_{i2} = c_{i0,\gamma 1} a_{i0} c_{\gamma 1,i2} \tag{11}$$

or:

$$A_{i2} N_{i2} = c_{i0,\gamma 1} A_{i0} N_{i0} c_{\gamma 1,i2} \tag{12}$$

And the transmittance through the composite plasmonic waveguide is obtained as:

$$Transmittance(z = L) = |A_{i2}/A_{i0}|^2 = |\sum_{\gamma=i,j,m} c_{i0,\gamma 1} c_{\gamma 1,i2} (N_{i0}/N_{i2})|^2 \tag{13}$$

or:

$$T = |\sum_{\gamma 1=i,j,m} C_{\gamma 1} exp(-\imath \alpha_{\gamma 1} L)|^2 \tag{14}$$

Where $C_{\gamma 1} = (I_{i0,\gamma 1} + I_{\gamma 1,i0})^2/(4 I_{i0,i0} I_{\gamma 1,\gamma 1})$ and L is length of a gold overlayer.

From Eq. (13) or Eq. (14) the transmittance through the composite-plasmonic waveguide structure presented here, can be calculated.

3. Simulation of expansion coefficients, device transmittance and surface intensity

In this section, the complex expansion coefficients relating the fields in the gold-coated and the uncoated regions of the device shown in Fig. 1 are evaluated as a function of superstrate index. These are then used to calculate the composite device transmittance vs. superstrate index for a range of gold lengths, L, which are compared with results for slab waveguides [10]. The behavior of the optical intensity at the surface of the gold film, of importance in surface-enhanced phenomena, is then described, illustrating the impact of the phase of the expansion coefficients and the beating and attenuation behavior of the modes in the gold-coated region. The modal quantities used are those determined in Section 2.1, and the composite waveguide structure is simulated at a wavelength of 633nm to allow ready comparison with literature.

3.1. Expansion coefficients

The expansion coefficients derived in Section 2.2 are, in general, complex. At the 1^{st} waveguide discontinuity ($z = 0$), the expansion coefficients provide the amplitude and phase of excitation of each eigenmode in the gold-coated region (Region 1: the HDM, SPP-s and SPP-a modes). The expansion coefficients at the 2^{nd} discontinuity at $z = L$ provide the contributions of the HDM, SPP-s and SPP-a eigenmodes to the power in the output dielectric waveguide as shown in Fig. 1, Region 2. Figure 5 shows the amplitude and phase of the complex expansion coefficients at the 1^{st} discontinuity ($z = 0$) and 2^{nd} discontinuity ($z = L$), for HDM, Figs. 5(a)-5(b), SPP-s Figs. 5(c)-5(d), and SPP-a Figs. 5(e)-5(f). It is observed that the amplitude and phase of the expansion coefficients between the same modes at the two interfaces ($z = 0$ and $z = L$) are different, with the amplitudes at the 2^{nd} discontinuity being consistently smaller. Fig. 5(a) also shows that the amplitude of the HDM mode at the 1^{st} step acquires values larger than 1 for a superstrate index around 1.36. This does not violate power flow conservation. To verify this the total power flow across the 1^{st} discontinuity has been calculated. Fig. 6 shows the P_1/P_0 ratio, where $P_0 = P_z(z = 0^-)$ and $P_1 = P_z(z = 0^+)$, as a function of the superstrate index. It is shown that despite the calculated DM/HDM expansion coefficient being higher than unity, P_1 is always lower than P_0. The difference $P_0 - P_1$ gives a measure of the losses due to the excitation of radiation and leaky modes at the discontinuity, which are not explicitly calculated in this study.

#235802 - $15.00 USD Received 11 Mar 2015; revised 8 May 2015; accepted 15 May 2015; published 22 May 2015

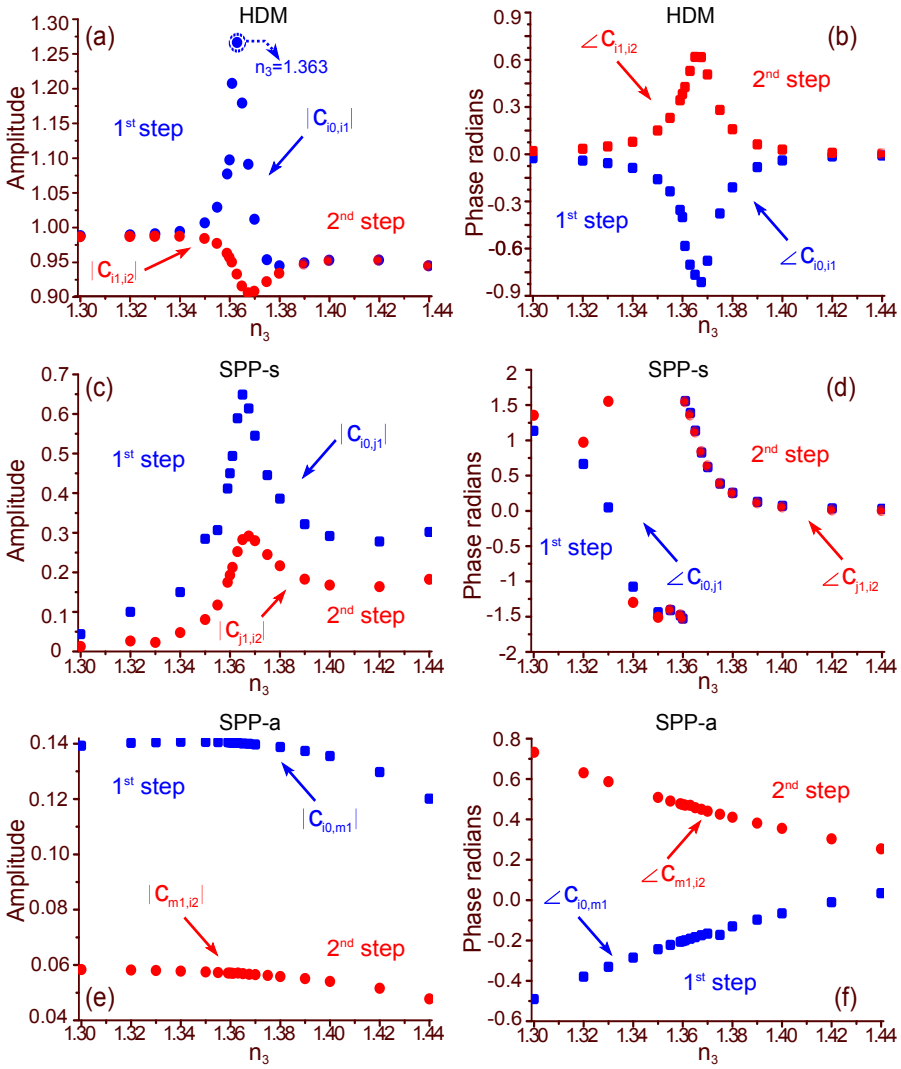

Fig. 5. Calculated expansion coefficients between the DM in region 0 and the eigenmodes in regions 1, at $z = 0$ (blue) and similarly between the modes in regions 1 and 2 at $z = L$ (red). From Eqs. (9-10): (a), (c), (e) amplitude and (b), (d), (f) phase. Note: The superstrate index, n_3 where the HDM mode is most strongly excited is labeled in (a).

#235802 - $15.00 USD Received 11 Mar 2015; revised 8 May 2015; accepted 15 May 2015; published 22 May 2015

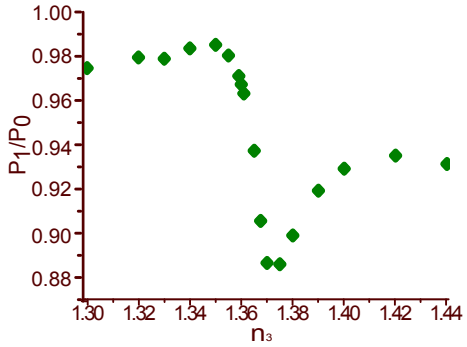

Fig. 6. Ratio of power in region 1 (P_1) to power in region 0 (P_0) at $z = 0$.

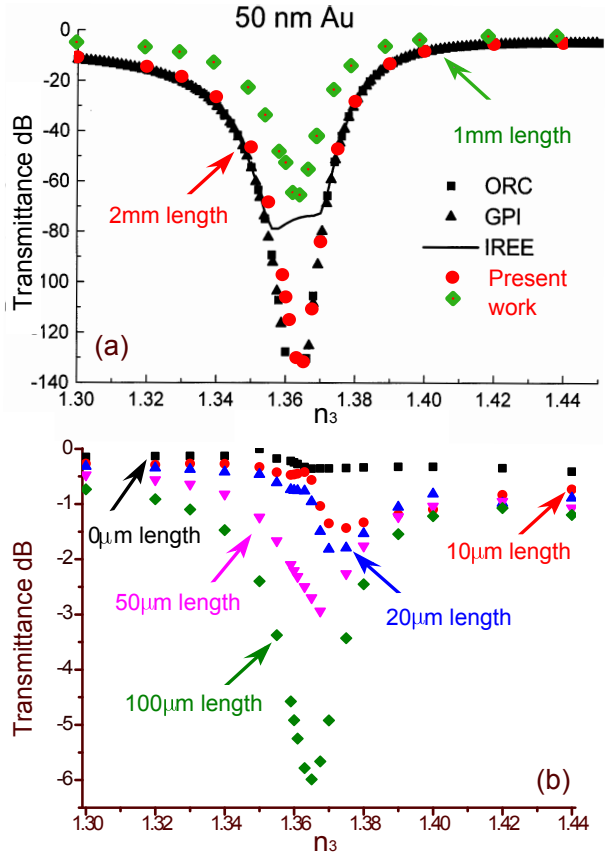

Fig. 7. (a) Calculated optical transmittance for $L = 2$mm based on our model presented in this paper compared to Fig. 7(c) from [10] and of $L = 1$mm; (b) comparison of $L = 0, 10, 20, 50$ and 100μm interaction lengths.

#235802 - $15.00 USD Received 11 Mar 2015; revised 8 May 2015; accepted 15 May 2015; published 22 May 2015

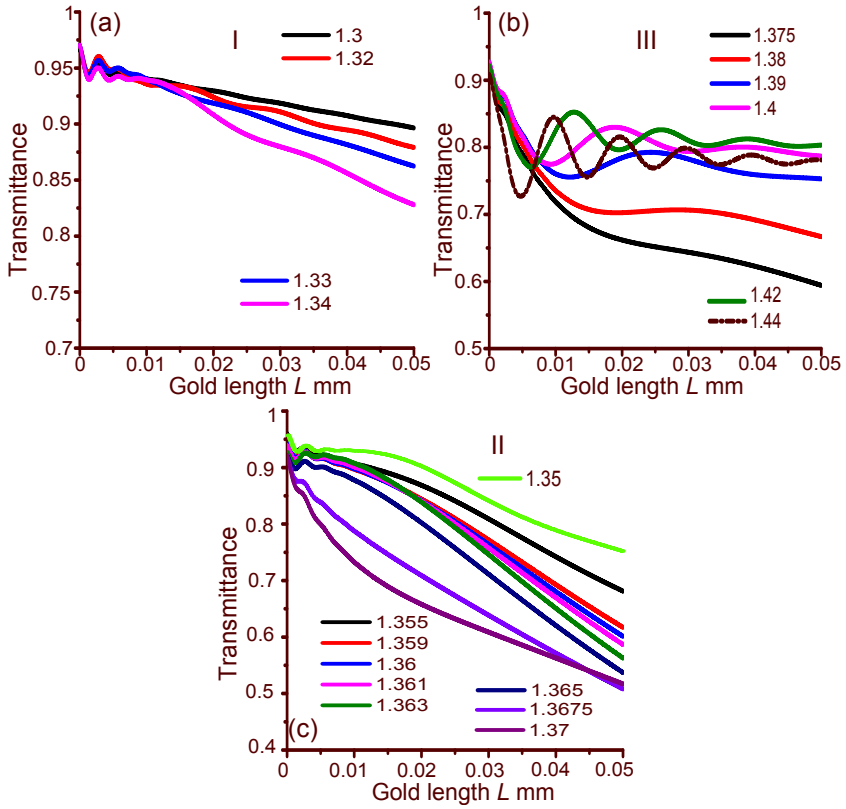

Fig. 8. (a) Calculated transmittance as a function of the gold length L in the zones: (a) I, (b) III and (c) II, for the indices of n_3.

3.2. *Optical transmittance*

Equation (14) yields the total optical transmittance of the composite device, neglecting back-scattered light and multiple reflections [10]. At the boundary between a pure dielectric waveguide and a waveguide coated with a thin gold film, these reflections have been shown to be very weak (below -60dB) [15].

The optical transmittance of the composite structure is defined primarily by the losses of the complex HDM in the gold-coated region $0 < z < L$. The SPP-s and SPP-a modes have very high modal attenuation of order 10^4dB/cm, as shown in Fig. 4(b), and therefore contribute little to the device transmittance; this is especially true for the SPP-a mode. The transmittance is then largely dependent upon the behavior of the HDM mode, due to its relatively low attenuation and large expansion coefficient. The device transmittance, T, as a function of superstrate index is shown in Fig. 7 for a variety of gold lengths, L. Figure 7(a) shows the calculated optical transmittance with $L = 2$mm, based on our model, superimposed upon the values for a slab waveguide presented in [10], showing excellent agreement, though with a small shift due to the channel nature of the waveguide modeled here. A 4x2μm core waveguide is a good approximation to the channel waveguide used in [16] and Fig. 7(a) shows a small change in resonance position when compared with the slab waveguide model. Figure 7(b) shows the device transmittance for shorter interaction lengths L, ranging from 100μm down to 10μm, resulting in increasing transmittance as expected. For $L > 100\mu$m the optical transmittance closely follows the modal attenuation profile of the HDM and the peak loss scales with the 70dB/mm loss co-

#235802 - $15.00 USD Received 11 Mar 2015; revised 8 May 2015; accepted 15 May 2015; published 22 May 2015

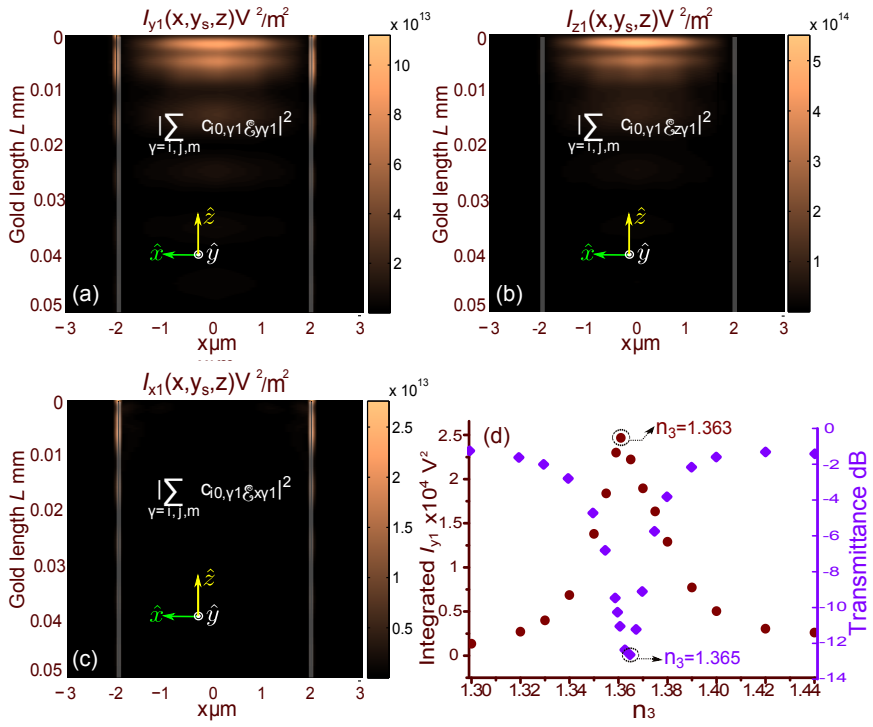

Fig. 9. Mapped surface intensity: (a) y component, (b) z component and (c) x component based on Eq. (15) along 50μm gold length for a superstrate index of 1.44 and (d) integrated surface intensity and transmittance for a $L = 200\mu$m gold length vs. n_3. Note: The superstrate indices, n_3 which yield the minimum in transmittance and the maximum in integrated surface intensity are labeled in (d).

efficient as shown in Fig. 4(b). However, it is notable that the shape of the resonance is strongly distorted for $L < 50\mu$m. This is because, for shorter lengths, significant power remains in the highly lossy SPP-s mode at $z = L$, which then contributes to the transmittance of the device. As the HDM and SPP-s modes propagate with different velocities and as their effective indices change differentially with superstrate index, these two modes interfere constructively or destructively at the $z = L$ plane when exciting the output waveguide, as the superstrate index changes, distorting the shape of the T vs n_3 curve. The beat-length depends on the N_{eff} difference between the HDM and SPP modes shown in Fig. 4(a). To illustrate this behavior, the device transmittance is plotted as a function of L for different superstrate indices in Fig. 8, grouped into superstrate index zones below resonance (I), near resonance (II) and above resonance (III). For all refractive indices the transmittance shows oscillations with L for small values of Ls, illustrating the (HDM-SPP) modal beat length for a particular value of n_3. For $L > 50\mu$m the beating behavior ceases because the power in the SPP-s mode is no longer significant. For superstrate indices of $1.3 - 1.32$, Fig. 8(a), the beating behavior is dominated by the HDM-SPP-a modes because the SPP-s mode is extremely weakly excited, Fig. 5(c), but the beating dies out over a length of a few microns because of the high loss of the SPP-a mode. In contrast, for superstrate indices nearer the resonance, Fig. 8(b) $n_3 > 1.39$, the oscillations are particularly pronounced because the excitation efficiency of the SPP-s mode is significant, Fig. 5(c), and they persist to a length of nearly 50μm because the loss of the SPP-s mode is relatively low. In the case of the highest index modeled ($n_3 = 1.44$) the transmittance reaches a

#235802 - $15.00 USD Received 11 Mar 2015; revised 8 May 2015; accepted 15 May 2015; published 22 May 2015

near-constant value with length from L of about 50μm, because the remaining HDM has a loss of only 1.74 dB/mm which is negligible over the 50μm length shown.

3.3. *Surface intensity*

The surface intensity over a known waveguide length for a given input power is an important parameter to assess the sensitivity of evanescent waveguide sensors, particularly for biosensors where chemical processes in monomolecular films are studied and in general for design of devices with improved signal to noise ratio. In the case of a channel waveguide, the intensity is normally integrated across the width of the waveguide, in order to arrive at a performance measure for a specific device length. In this section, the behavior of the intensity at the surface of the gold film ($y_s = d + t$) is studied:

Surface intensity (I) which is calculated as:

$$I(x, y_s, z) = |E(x, y_s, z)|^2 = |\sum_{\gamma=i,j,m} c_{i0,\gamma 1} \mathscr{E}_{\gamma 1}(x, y_s, z)|^2. \tag{15}$$

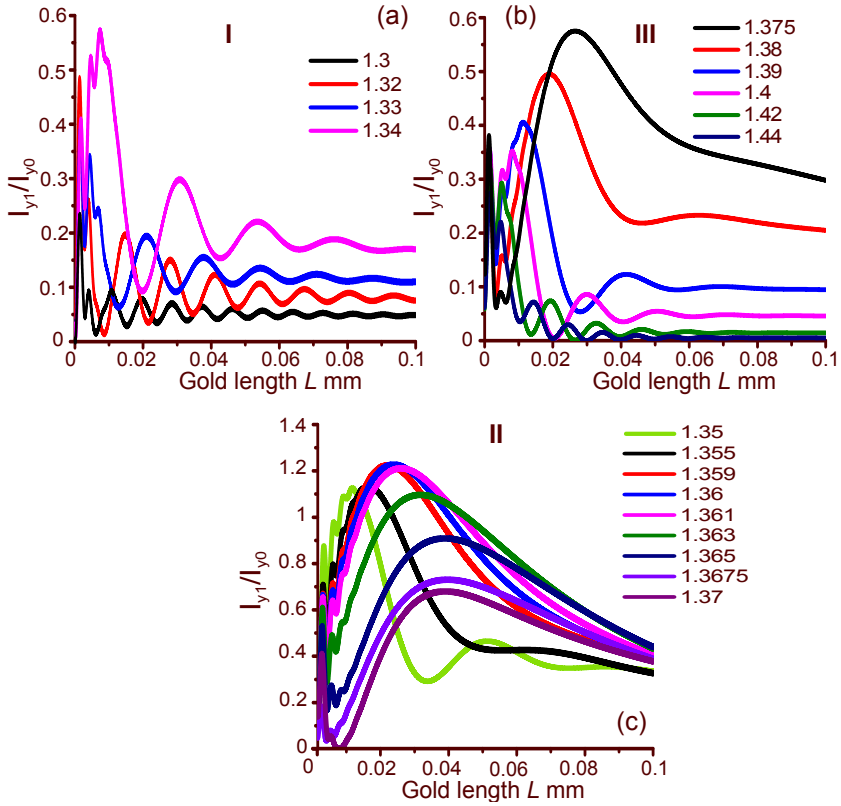

Fig. 10. Calculated surface intensity profiles at $x = 0$ and along $L = 100\mu$m based on Eq. (15) in zones: (a) I, (b) III and (c) II.

3D plots of $|E_y|^2$, $|E_z|^2$, and $|E_x|^2$ at the gold surface are shown in Figs. 9(a)-9(c), respectively. The modal beating behavior is clearly visible. The surface intensity integrated across the full width of the waveguide and along the length from $z = 0$ to $z = 200$ μm for varying superstate index is shown in Fig. 9(d), yielding the highest integrated surface intensity at $n_3 = 1.363$ which

#235802 - $15.00 USD Received 11 Mar 2015; revised 8 May 2015; accepted 15 May 2015; published 22 May 2015

corresponds to the highest excitation (expansion coefficient) of the HDM mode as in Fig. 5(a) close to the surface plasmon resonance.

Figure 10 shows the surface intensity at the center of the waveguide ($y = d + t;\ x = 0$) along a 100 micron length for the superstrate index values and regions used in Fig. 8. The surface intensity is not maximum at the start of the gold film (z=0) but after a distance of $10 - 30\mu$m into the gold-coated region. This is because the phases and amplitudes of the HDM mode and the SPP-s and SPP-a modes at $z = 0$ are such that they interfere destructively across the thin metal film and the total field matches the dielectric mode (DM) closely. The superimposed SPP modes are extinguished beyond a propagation length of about 50μm, leaving the HDM to propagate alone. Around the resonance, HDM shows strong localization across the thin metal film which results in the observed increased surface intensity. It is observed that the highest surface intensity is achieved for superstrate refractive index of $n_3 = 1.363$, which corresponds to the highest value of HDM expansion coefficient. Also, in order to fully utilize this surface intensity maximum in a sensor application, the minimum length of the gold thin film should be at least $L \sim 25\mu$m.

4. Conclusion

Hybrid devices combining dielectric waveguides with plasmonic structures have many applications in photonic circuitry. A detailed theoretical study of a composite-plasmonic waveguide structure based on channel waveguides is given in this paper, yielding detailed information on the excitation of modes in the composite structure from an input dielectric waveguide, their propagation over the gold-coated region, the transmittance of the device into an output dielectric waveguide, and the optical intensity at the surface of the gold film. It was observed that modal beating in the gold-coated region, which strongly affects surface intensity and transmittance, can be controlled through the superstrate index, and that the transmission and surface intensity behavior is dominated by the behavior of the hybrid dielectric-plasmonic mode (HDM) in terms of its excitation and attenuation. The behavior of the complex expansion coefficients, coupling the modal fields in the gold-coated and uncoated waveguide regions, is studied near the resonance as the superstrate refractive index is varied, and it is shown that the magnitudes of these are dissimilar for the input and output transitions (dielectric waveguide into composite waveguide and composite waveguide out to dielectric waveguide); nonetheless power flow across interfaces is shown not to violate power conservation principles and accounts for radiation and other scattering losses. Device transmittance is shown to agree well with the published literature for slab waveguides, with a small deviation due to the channel nature of the waveguides modeled here.

The charge oscillation, plasmons, are localized in the direction perpendicular to the metal boundary and are accompanied by a mixed transversal and longitudinal electromagnetic field having maximum in the surface of metal boundary, typically for surface waves. Therefore, surface plasmons are sensitive to surface properties. The surface intensity is important for many applications in sensing, spectroscopy and nonlinear optics. Here, the intensity at the surface of the gold film is mapped, showing the beating behavior of the modes in the gold-coated region and clarifying the regions of highest surface intensity and enabling design of devices in terms of the maximum and minimum useful length of the gold film. It is observed that the maximum surface intensity integrated over the gold surface occurs at the value of superstrate index 1.363, where the HDM mode is most strongly excited. This superstrate index is different from the position of minimum transmittance at superstrate index of 1.365, which is defined by the maximum HDM propagation loss (which occurs here at the superstrate index of 1.365) and the beating with the SPP modes. This theoretical study enables clear understanding of the complex behavior of modes in composite dielectric-plasmonic waveguides and design of optimised sen-

#235802 - $15.00 USD Received 11 Mar 2015; revised 8 May 2015; accepted 15 May 2015; published 22 May 2015

sitive miniature devices for refractometry, evanescent vibrational spectroscopy and plasmonic devices for all-optical processing, harnessing the advantages of both dielectric and plasmonic waveguides. The model developed is general and can be used to design and optimize composite waveguides with more complex overlayer structures.

Appendix: relation between eigenmodes at an abrupt step

By substituting Eq. (5) and Eq. (6) into Eq. (4) we obtain:

$$a_{i0}a_{\gamma 1}\int_{-\infty}^{\infty}\int_{-\infty}^{\infty}(\bar{\mathscr{E}}_{i0}\times\bar{\mathscr{H}}_{\gamma 1})_z+(\bar{\mathscr{E}}_{\gamma 1}\times\bar{\mathscr{H}}_{i0})_z\mathrm{dxdy}=a_{\gamma 1}^2\int_{-\infty}^{\infty}\int_{-\infty}^{\infty}(\bar{\mathscr{E}}_{\gamma 1}\times\bar{\mathscr{H}}_{\gamma 1})_z+(\bar{\mathscr{E}}_{\gamma 1}\times\bar{\mathscr{H}}_{\gamma 1})_z\mathrm{dxdy} \tag{16}$$

To obtain a relation between eigenmodes at an abrupt step:

$$a_{i0}(I_{i0,\gamma 1}+I_{\gamma 1,i0})=a_{\gamma 1}2I_{\gamma 1,\gamma 1} \tag{17}$$

$$a_{\gamma 1}=a_{i0}(I_{i0,\gamma 1}+I_{\gamma 1,i0})/(2I_{\gamma 1,\gamma 1}) \tag{18}$$

Where:

$$I_{i,\gamma}=\int_{-\infty}^{\infty}\int_{-\infty}^{\infty}(\bar{\mathscr{E}}_i\times\bar{\mathscr{H}}_\gamma)_z\mathrm{dxdy}=\int_{-\infty}^{\infty}\int_{-\infty}^{\infty}(\mathscr{E}_{xi}\mathscr{H}_{y\gamma}-\mathscr{E}_{yi}\mathscr{H}_{x\gamma})_z\mathrm{dxdy} \tag{19}$$

N_δ can then be expressed as:

$$N_\delta=(2/\Re(I_{\delta,\delta}))^{1/2} \tag{20}$$

Which is:

$$A_{\gamma 1}N_{\gamma 1}=A_{i0}N_{i0}(I_{i0,\gamma 1}+I_{\gamma 1,i0})/(2I_{\gamma 1,\gamma 1}) \tag{21}$$

Acknowledgments

The research leading to these results has received funding from the European Research Council under the European Union's Seventh Framework Programme (FP7/2007 -2013) ERC grant agreement no. 291216 Wideband Integrated Photonics for Accessible Biomedical Diagnostics (JSW), support from an Outstanding Woman in Science Award (BGU, Israel) (AK) and partial support from the EPSRC Centre for Innovative Manufacturing in Photonics (EP/H02607X/1) (MNZ).